

Article

Electronic Structure and Hardness of Mn_3N_2 Synthesized under High Temperature and High Pressure

Shoufeng Zhang¹, Chao Zhou¹, Guiqian Sun¹, Xin Wang^{1,*}, Kuo Bao¹, Pinwen Zhu¹, Jinming Zhu¹, Zhaoqing Wang¹, Xingbin Zhao², Qiang Tao¹ , Yufei Ge¹ and Tian Cui^{1,2,*}

¹ State Key Laboratory of Superhard Materials, College of Physics, Jilin University, Changchun 130012, China

² Institute of High Pressure Physics, School of Physical Science and Technology, Ningbo University, Ningbo 315211, China

* Correspondence: wang-xin@jlu.edu.cn (X.W.); cuitian@jlu.edu.cn (T.C.)

Abstract: The hardness of materials is a complicated physical quantity, and the hardness models that are widely used do not function well for transition metal light element (TMLE) compounds. The overestimation of actual hardness is a common phenomenon in hardness models. In this work, high-quality Mn_3N_2 bulk samples were synthesized under high temperature and high pressure (HTHP) to investigate this issue. The hardness of Mn_3N_2 was found to be 9.9 GPa, which was higher than the hardness predicted using Guo's model of 7.01 GPa. Through the combination of the first-principle simulations and experimental analysis, it was found that the metal bonds, which are generally considered helpless to the hardness of crystals, are of importance when evaluating the hardness of TMLE compounds. Metal bonds were found to improve the hardness in TMLEs without strong covalent bonds. This work provides new considerations for the design and synthesis of high-hardness TMLE materials, which can be used to form wear-resistant coatings over the surfaces of typical alloy materials such as stainless steels. Moreover, our findings provide a basis for establishing a more comprehensive theoretical model of hardness in TMLEs, which will provide further insight to improve the hardness values of various alloys.

Keywords: hardness; Mn_3N_2 ; electronic structure; high temperature and high pressure synthesis



Citation: Zhang, S.; Zhou, C.; Sun, G.; Wang, X.; Bao, K.; Zhu, P.; Zhu, J.; Wang, Z.; Zhao, X.; Tao, Q.; et al. Electronic Structure and Hardness of Mn_3N_2 Synthesized under High Temperature and High Pressure. *Metals* **2022**, *12*, 2164. <https://doi.org/10.3390/met12122164>

Academic Editors: Shinichiro Adachi, Francesca Borgioli and Thomas Lindner

Received: 9 November 2022

Accepted: 13 December 2022

Published: 16 December 2022

Publisher's Note: MDPI stays neutral with regard to jurisdictional claims in published maps and institutional affiliations.



Copyright: © 2022 by the authors. Licensee MDPI, Basel, Switzerland. This article is an open access article distributed under the terms and conditions of the Creative Commons Attribution (CC BY) license (<https://creativecommons.org/licenses/by/4.0/>).

1. Introduction

Hardness is a well-known concept for which several models have been proposed [1–4], but the internal physics of this property are not well understood. This limited understanding of hardness considerably hinders the design and knowledge of superhard materials. Since the idea of combining high-bulk-elastic-modulus transition metals and high-shear-modulus light elements was proposed [5–7], many transition metal light element (TMLE) compounds have been synthesized and measured [2,8–11]. For TMLEs such as ReB [12–14], WC [15], and TiN [16], most of their measured hardness values deviate from the theoretically predicted values. Therefore, widely used hardness models might not fully describe all the important physical factors in these systems.

For the application of typical alloys limited by their hardness and chemical stability of the surface, novel wear-resistant and rust-resistant coating materials are required [17,18]. Transition metal nitrides have been extensively studied owing to their excellent physical and chemical properties [19]. In 2019, we found that the interactions between metal atoms might benefit the hardness of transition metal nitrides (TMNs) and TMLEs in our study on WN and CrN [20]. Compared with the outer valence electrons of Cr and W, both the semi-filled *d* orbital and fully filled *s* orbital electron clouds of Mn would better improve the interactions between metal atoms. Although the latest results show that Mn_3N_2 is mechanically unstable [21], the hardness of Mn_3N_2 could not be obtained from the elastic model of bulk materials [13], which are good candidates for investigating hardness. Based

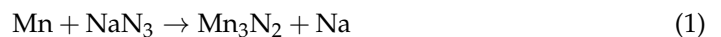
on the hardness results obtained from experiments, the existing hardness theories could be improved.

Many TMNs have been synthesized using methods such as film deposition [22], magnetron sputtering [23], and hermetic sintering [24], and acceptable results have been achieved via investigation of the obtained samples. However, the precise measurement of hardness has not yet been achieved because of the absence of high-quality synthesized bulk samples. The high temperature and high pressure (HTHP) technique is an effective synthesis approach to prepare high-quality bulk samples, especially TMNs. The triple covalent bond of N-N is one of the strongest chemical bonds, and it is difficult to synthesize TMNs until a mature high-pressure metathesis reaction has been achieved [20,25,26]. Meanwhile, the application of high pressure is effective in preventing nitrogen from escaping the experimental system. Further, HTHP synthesis is an effective approach to prepare fine bulk TMN samples [27,28]. After obtaining high-quality bulk samples, the precisely measured hardness of Mn_3N_2 could be easily obtained.

In this study, we investigate the preparation and simulation of Mn_3N_2 samples, discuss the experimental and simulated results, and then provide our conclusions concerning the hardness evaluation of this material.

2. Experiment and Simulation Details

We prepared our samples with Mn and NaN_3 powders (both 99.95% pure) at a molar ratio slightly lower than 3:2. NaN_3 was in excess in the raw material to ensure a sufficient N_2 atmosphere. During the grinding process, it should be noted that NaN_3 exhibits a certain explosiveness under severe vibrations, and intense impacts should be avoided. The mixture was pressed into cylinders before being sealed in *h*-BN capsules, and the cylinders were assembled and subjected to HTHP with a cubic China-type SPD6 × 600T apparatus. The sample was compressed under 5 GPa, heated to 1800 °C, and held under this thermal condition for 30 min. Then, the heating current was stopped, and the pressure was released to ambient conditions over approximately 9 min.



The elemental substance Na very easily reacts with water and oxygen in air to generate sodium ions. To obtain samples with less impurities and better density, the primary samples were ground to powder and washed with water to eliminate ionic Na impurities. The centrifuged and dried powder was then subjected to second sintering with China-type SPD6 × 600T, where the powder was held at 5 GPa and 700 °C for 20 min.

The samples were characterized by X-ray diffraction (XRD) for phase identification on a Rigaku SmartLab SED/teX Ultra250 X-ray diffractometer ($CuK_{\alpha 1}$ radiation, $\lambda = 1.5404 \text{ \AA}$) in the 2θ range of 10° to 90° with a step size of 0.01° , and the X-ray photoelectron spectrum (XPS) measurements were conducted after it was cleaned by Ar⁺ sputtering within 180 s. The surface morphology of the sample was obtained by scanning electron microscopy (SEM) and energy-dispersive spectrometry (EDS). HV-1000 ZDT microhardness equipment was used to test the hardness of the sample after the second sintering.

Here, structural relaxation and property calculations were performed within a density functional theory (DFT) framework and the projector-augmented wave (PAW) [29], as implemented in the Vienna ab initio simulation package (VASP) [30]. Perdew–Burke–Ernzerhof (PBE) [31] generalized gradient approximation was used to process the exchange–correlation potential. We set an energy cutoff of 600 eV for plane-wave basis and gamma-centered k mesh spacing as $2\pi \times 0.03 \text{ \AA}^{-1}$ in the calculations. The forces between the atoms were converged within 0.01 eV/\AA in the relaxation. Mn 4s, 3d, and 3p electrons as well as N 2p and 2s electrons were explicitly calculated and not included in the pseudopotential. Crystal Orbital Hamilton Population (COHP) [32] and Crystal Orbital Bond Index (COBI) [33] were calculated using the LOBSTER package.

3. Results and Discussion

The powder XRD and Rietveld fitting [34] of our samples are shown in Figure 1. Comparing the sample with the standard crystal card, the XRD spectrum of the sample fits that of Mn_3N_2 . The samples are crystalline and single-phase, and the confidence factors wRp and Rp are less than 3%. The structure of the sample was studied from two directions to investigate the connections between the internal parts of the lattice. As is evident from the structure shown in Figure 1, six Mn atoms are connected around each N atom, and N atoms are connected around each Mn atom. The chemical formula of the crystal is Mn_3N_2 , and the space group of the crystal is $I4/mmm$, $a = 2.9769(1) \text{ \AA}$, $b = 2.9769(1) \text{ \AA}$, and $c = 12.2646(5) \text{ \AA}$. More information concerning these crystals is given in Table 1.

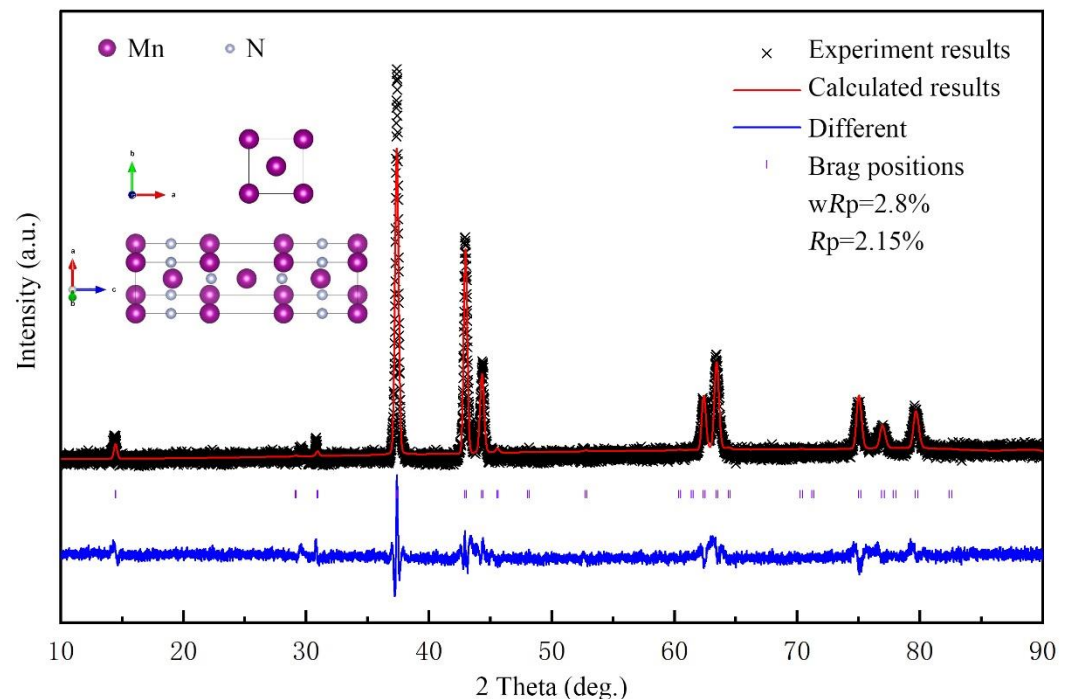


Figure 1. Powder (R3C4) XRD test pattern of crystal. \times is the test value of the experiment, the red line is the calculated fitting value, and the blue line is the difference between the two.

Table 1. Experimental data and crystal details obtained from Rietveld refinement.

Identification Code	Mn_3N_2
Space group	$I4/mmm$
Unit cell dimensions (\AA)	$a = 2.9769 \text{ \AA}$,
	$c = 12.2646 \text{ \AA}$,
	$a/b = 1$
Volume (\AA^3)	$b/c = 0.2427$
	108.69

The SEM evaluation of the morphology of the samples showed that our samples are compact and of sufficient quality for the hardness test, as shown in Figure 2. Here, (a,b) relate to the morphology of the samples synthesized during the first preparation, while (c,d) relate to the morphology of the samples sintered for a second time. Evidently, after the initial synthesis, the sample showed porosity and incompact characteristics, which may be due to the outgassing of NaN_3 during the initial reaction. In addition, after the initial synthesis of the sample, the crystallization degree of the sample was poor, and the crystallization was not obvious. After the secondary sintering treatment, the compactness of the sample was significantly improved, and no obvious pores were visible on the micro scale, which demonstrated that the samples met the standard for hardness measurements.

In addition, the density achieved after secondary sintering was approximately 20% higher than the primary synthesized samples. After secondary sintering, the density of the samples reached approximately 97%, which may improve the accuracy of the hardness test results.

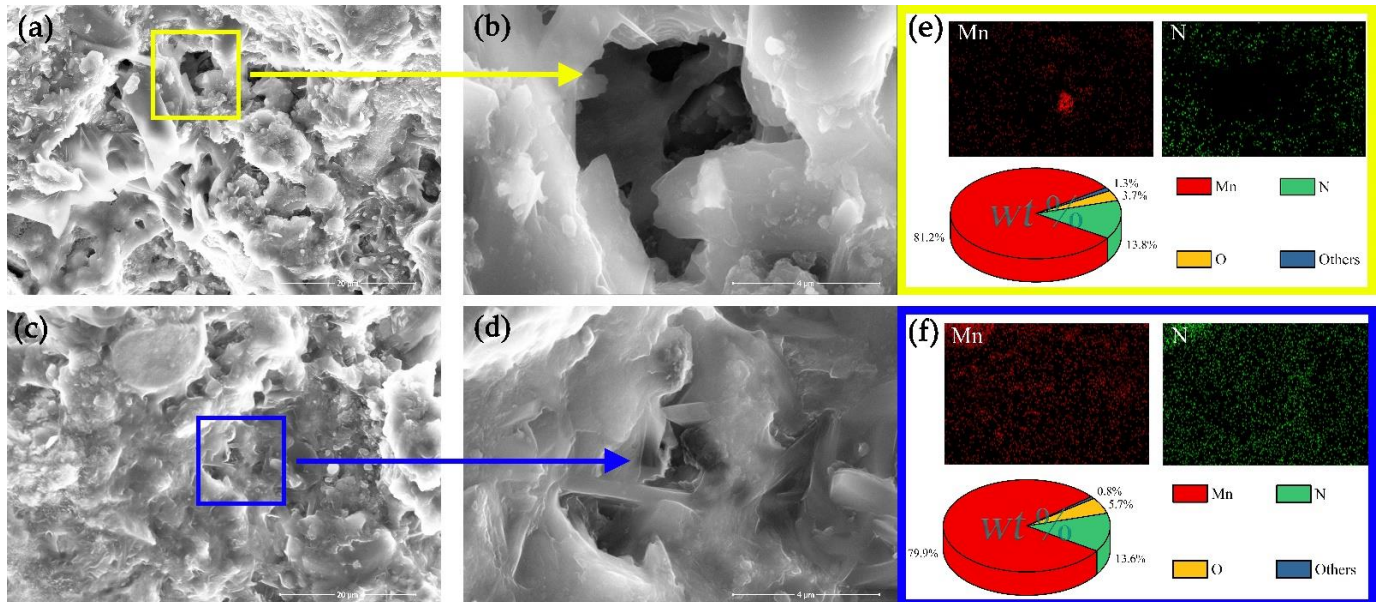


Figure 2. (a–d) show the low- and high-magnification SEM images of Mn_3N_2 bulk materials. (a,b) are the samples after primary synthesis, and (c,d) are the samples after secondary sintering. (b) is the magnification area of the yellow box in (a); (d) is the magnification area of the blue box in (c). (e) Element distribution diagram and element content diagram of yellow box of initial synthesis by EDS; (f) element distribution diagram and element content diagram of blue box of initial synthesis by EDS.

Meanwhile, the EDS analysis of the elemental distribution in the samples after secondary sintering indicated that the Mn and N atoms were more evenly distributed. Other elements were obviously reduced after secondary sintering. Considering the error range of the EDS analysis instrument, we believe that Na is no longer present in the samples after secondary sintering. However, a significant increase in O content was observed between the initial synthesis and secondary sintering samples. This increase in O content may be due to the grinding and washing of samples during secondary sintering.

To determine whether the sample was oxidized to form Mn-O, the XPS profiles were obtained, as shown in Figure 3. The N-1s spectrum and Mn-2p spectrum of Mn_3N_2 are plotted in Figure 3a,b, respectively. The fitted intensity demonstrates that the two peaks in the N-1s spectrum are located at binding energies of 397.18 and 397.28 eV. These two binding energies with a small difference reflect the binding state of N with Mn atoms at different positions in Mn_3N_2 . The binding energies of 652.23 and 640.43 eV on the 2p orbital of metal Mn represent the split energy levels of Mn $2p^{1/2}$ and Mn $2p^{3/2}$, respectively. The binding energies of 638.73 and 652.43 eV show the change in the valence states of the Mn atoms, which clarifies the mechanism of electron transference. Therefore, the electrons of the Mn atoms correspond to different states when forming different bonds. The XPS results show that the Mn-N bond is the main bond and state in Mn_3N_2 , and no O bonds are found, which indicates that this sample is antioxidative.

The Vickers hardness of the secondary sintered sample was evaluated, as shown in Figure 4. The applied load was increased from 0.49 N to 9.8 N. As the load increased, a downward trend was observed in the hardness. The trend slowed when the applied load reached 2.94 N and began to converge. As the external load was further increased, the hardness value slightly decreased but showed a generally moderate trend. Therefore, we

believe that the intrinsic hardness of the sample was recorded under a 9.8 N load, and the hardness value is 9.9 GPa.

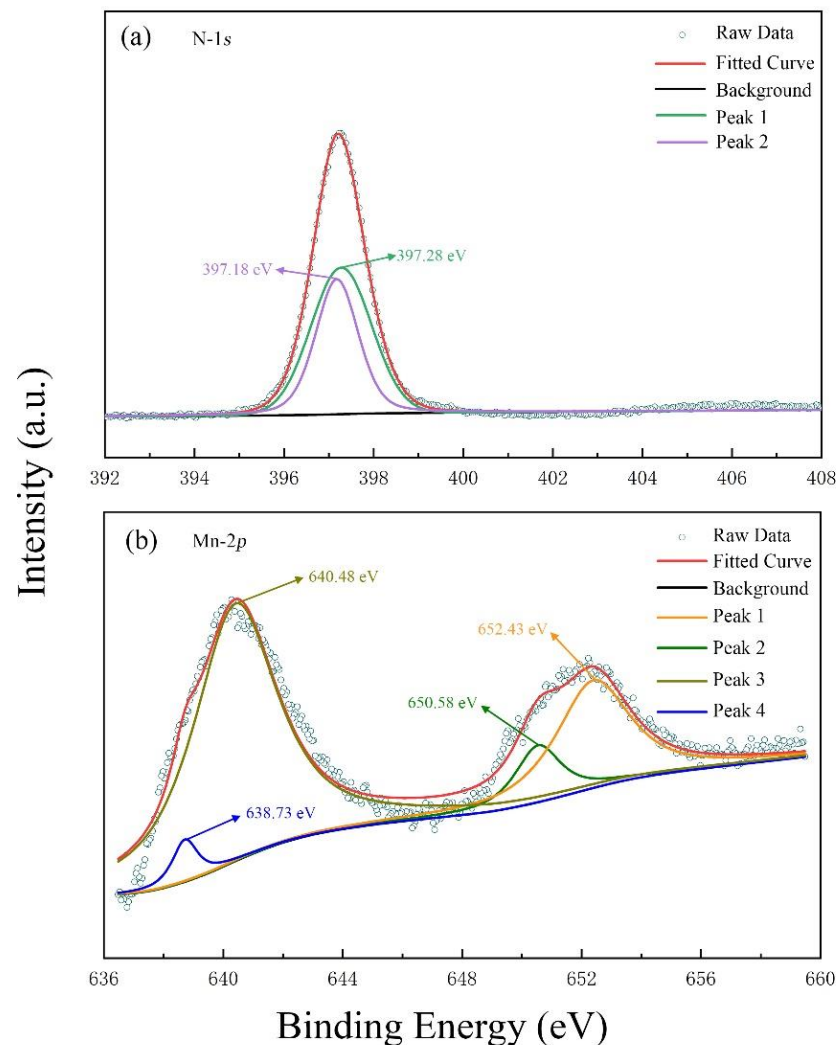


Figure 3. XPS spectra of the Mn_3N_2 sample. (a) N 1s spectrum with a binding energy of 392.0–408.0 eV; (b) Mn 2p spectrum with a binding energy of 636.48–659.48 eV.

The widely accepted hardness models by Gao et al. [2] and Guo et al. [3] are based on the assumption of the detailed analysis of chemical bonds. Guo further extended Gao's model by considering that the ionic bond in the crystal plays a major role in its hardness; therefore, we chose Guo's model to analyze the hardness of the sample. The following semi-empirical formula [3] was used:

$$Hv(\text{GPa}) = 1051N_e^{2/3}d^{-2.5}e^{-1.191f_i-32.2f_m^{0.55}}, \quad (2)$$

where N_e is the density of valence electrons in a single cell, $N_e = \frac{n_e}{v}$, n_e is the total number of valence electrons in a single cell, d is the distance between Mn and N in this system, f_i is the Phillips ionicity chemical bond, f_m is a defined factor of metal, $f_m = \frac{0.026D_F}{n_e}$, and D_F is the number of electrons on the Fermi surface according to our total density of states (TDOS) calculation; that is, $D_F \approx 24.885$. Then, a hardness $Hv \approx 7.01$ GPa was obtained.

However, the measured Vickers hardness of Mn_3N_2 is 9.9 GPa, which is approximately 40% higher than the predicted value. There exists a noticeable underestimation guided by Guo's model. Thus, the electronic structures of Mn_3N_2 were investigated. Figure 5 provides the density of states (DOS) of the crystal. The TDOS at the Fermi level (E_f) indicated that Mn_3N_2 was a metal. Below the Fermi level, the TDOS for Mn_3N_2 peaks were in two energy

regions. The first energy region, which was between -20 and -15 eV, was mainly induced by the s orbital bonding of N atoms with the d and p orbitals of Mn atoms. The second energy region, which was from -10 to 0 eV, was mainly due to the p orbital bonding of N atoms with the d orbitals of Mn. The contributions of the p orbitals of the Mn atoms were negligible. The s orbital of Mn was also ineffective for bonding. The major interaction in Mn_3N_2 was mainly the orbital hybridization of Mn and N atoms. At the Fermi level, the TDOS of Mn_3N_2 mainly comprised the d orbital electrons of Mn, and the electrons of N did not significantly contribute. Therefore, the d orbital electrons of the Mn atoms play a major role in this system, and the interaction of Mn–Mn contributes to the TDOS in Mn_3N_2 .

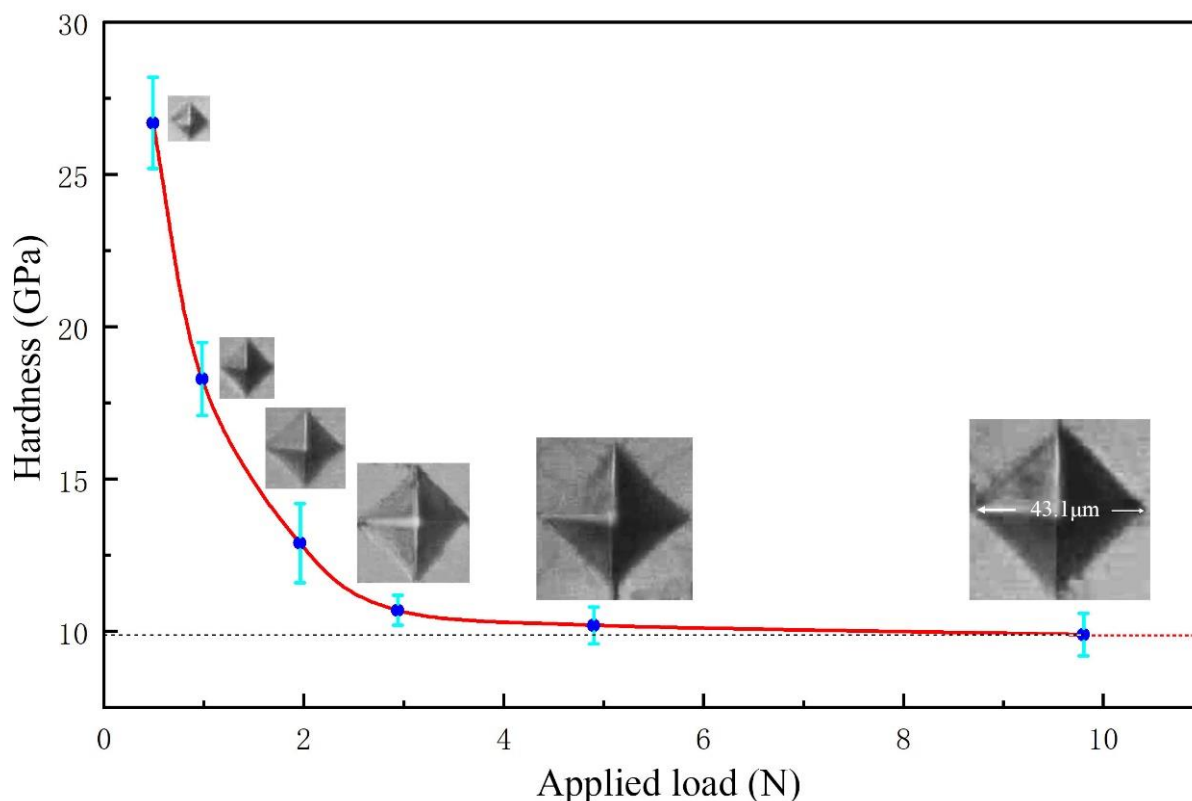


Figure 4. Vickers hardness for Mn_3N_2 , with the applied load ranging from 0.49 N (low load) to 9.8 N (high load). Typical optical images of the indentation are shown in the inset.

Figure 6 shows a 2D plane of the crystal calculated via electronic localization function (ELF) and intercepted along different crystal plane directions. A strong interaction occurred between the N atoms and the nearby Mn atoms, and the electrons that induced this interaction were mainly concentrated around the N atoms, which indicates electron localization. Almost no electrons were localized between N–N in the crystal, which indicates the occurrence of no interactions between N–N and no N–N covalent bonding in the sample. Additionally, electron localization between Mn–Mn was not ignored. In Figure 6, there is a certain probability of occurrence for electrons between Mn atoms. An evident conductive path forms between the Mn atoms, indicating a strong interaction between these atoms. Additionally, there may be strong Coulombic interactions along this path. It is well known that Coulombic interactions are very strong and may strongly contribute to deformation resistance. According to these findings and the DOS analysis results, the Mn_3N_2 metal mainly originates from the d orbitals of the Mn atoms, while the conductive path in the sample was also the route of sample formation.

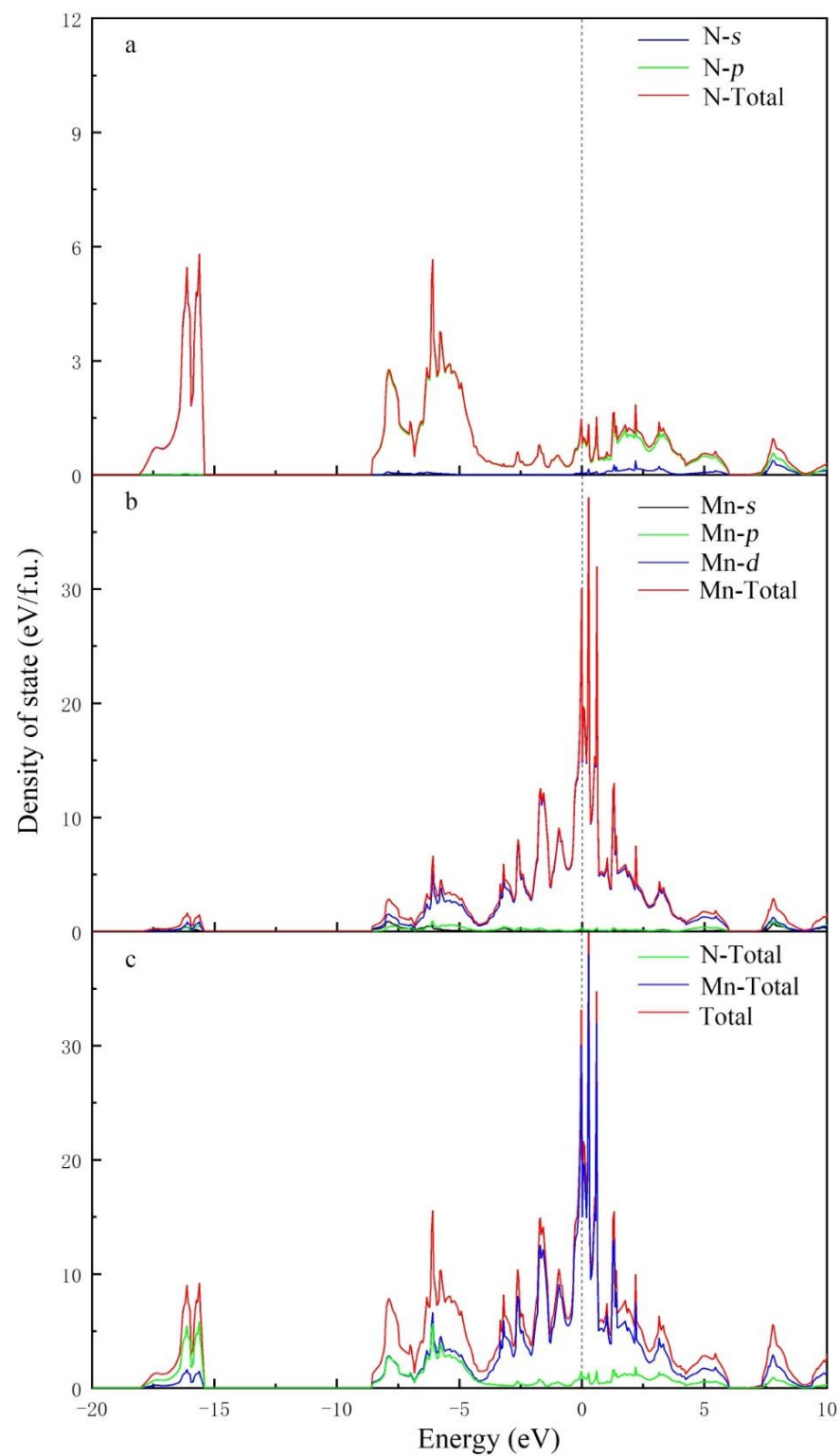


Figure 5. Total and partial density of states for Mn_3N_2 . (a) The *s* and *p* orbitals, and TDOS of N atoms. (b) The *s*, *p*, and *d* orbitals, and TDOS of Mn atoms. (c) The TDOS of Mn atoms, the total TDOS, and the TDOS of N atoms.

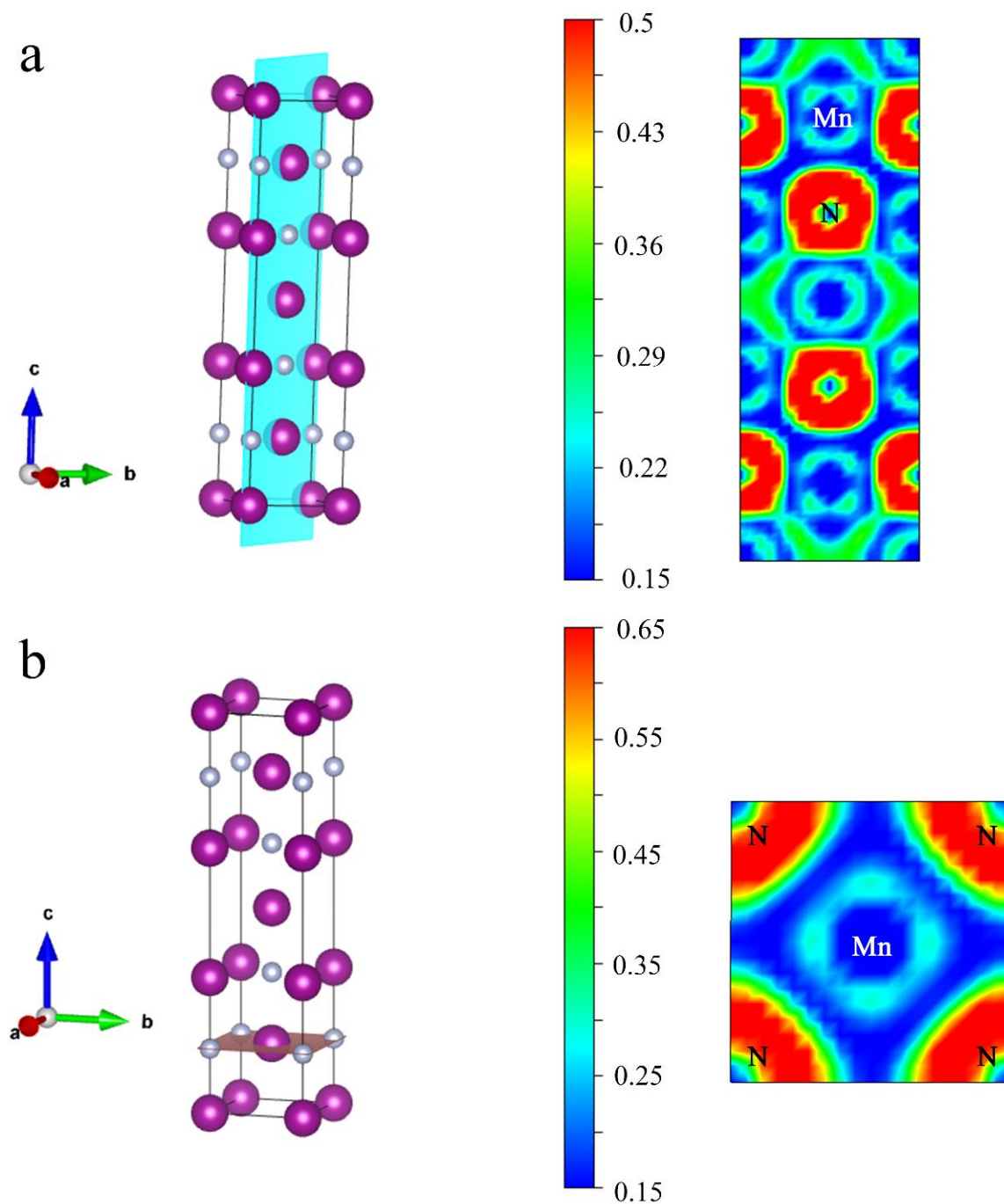


Figure 6. Electronic localization function for Mn_3N_2 . (a) Cutting along the (110) crystal plane with cyan and (b) cutting along the (001) crystal plane with caramel. Purple balls are Mn atoms, white ball are N atoms.

The COHP results used to investigate the bond strength of each specific bond in the crystal are shown in Figure 7, and the -ICOHP results are shown in Table 2. Owing to the different distances of Mn atoms among the different positions in the crystal, the interaction between the first neighboring atoms was stronger than that between the other atoms. Therefore, we only considered the nearest and next-nearest Mn atoms, and the nearest neighbor atoms between N-N were also considered.

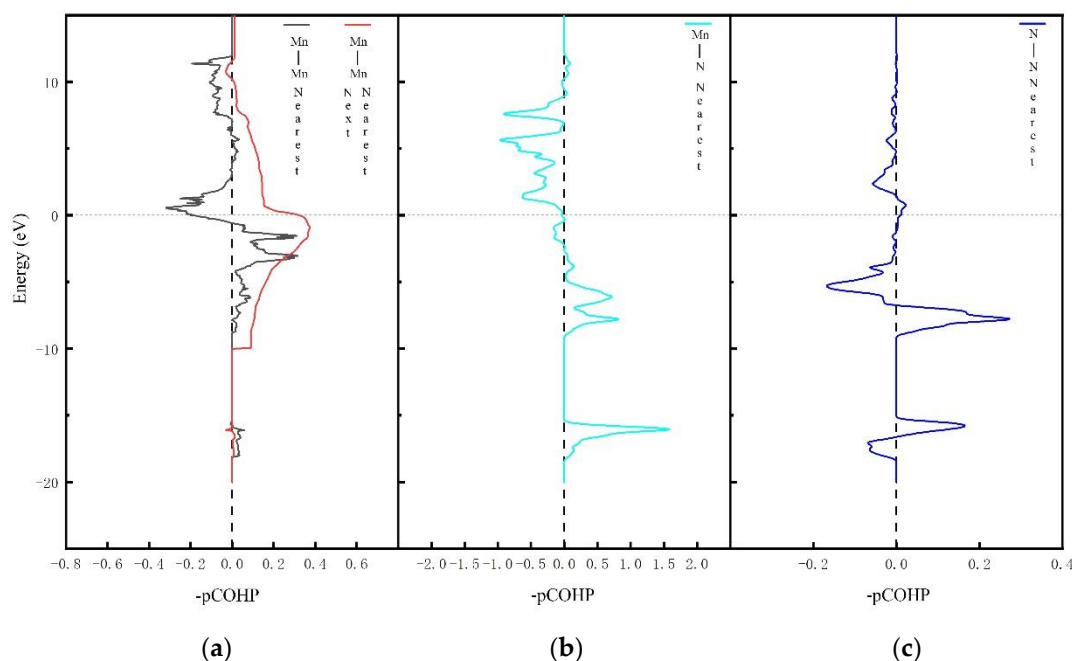


Figure 7. COHPs for Mn_3N_2 . The negative and positive COHP values denote bonding and antibonding interactions, respectively. (a) shows the COHPs for Mn–Mn nearest and next nearest; (b) is the COHP for Mn–N nearest; (c) is the COHP for N–N nearest.

Table 2. -ICOHP of bonds in Mn_3N_2 .

	Mn-N	Mn-Mn Nearest Mn-Mn Next-Nearest	N-N
-ICOHP (eV/pair)	3.0303	0.7319 0.5650	0.0975

The strength of the N–N bond in the crystal was near zero because the value of -ICOHP was only 0.097 eV/pair. The weak bonding of the N–N bond was mainly explained by the extremely long distance between these atoms such that the corresponding effect was difficult to achieve. Meanwhile, the DOS and ELF results showed that there was nearly no N–N covalent bond in the crystal, and the N–N covalent bonds could therefore be ignored in the subsequent analysis. The strongest bonds in the crystal were the ionic bonds between the Mn–N atoms, and the value of -ICOHP was 3.03 eV/pair. The bonding between Mn–N was extensive even at deep energy levels less than -15.0 eV, and almost no anti-bonding state was found below the Fermi surface, thereby indicating that the bonding between Mn–N was strong and the ionic bond of Mn–N played a crucial role in the crystal structure. The bonding between Mn–Mn in the crystal could also not be ignored. The -ICOHP values of Mn atoms at different positions and distances differed, but the approximate range was between 0.5 and 0.8 eV/pair. Moreover, most of the atoms were bonded below the Fermi level, which was conducive to the interactions between the Mn atoms. In the region of -10.0 to 0.0 eV, the bonding state between the Mn–Mn atoms was significant. Considering these results, we can provide a clear hypothesis regarding the bonding in the crystal. The Mn–N ionic bond plays a major role in the crystal hardness. Similar to metal crystals, electrons exist between Mn atoms, and the bonding state is strong. Moreover, no covalent N–N bonds are present in the crystal.

Different values between the theoretical hardness obtained using Guo’s semi-empirical formula and the actual hardness obtained by Hv testing will likely be observed for numerous TMLEs. For Mn_3N_2 , attention should be paid to the metal bonds originally considered helpless to the hardness of TMLEs when evaluating the hardness of these materials, as indicated by the results of the above investigations [2,3,35]. First-principle calculations

showed that the interactions between the Mn atoms in the Mn_3N_2 sample play an important role in the large DOS. Therefore, when an external shear force is applied, the common electrons in this crystal may slip. At this time, the electrons between the Mn–Mn metal atoms exhibit covalent bond-like properties, which strengthen the bonding between the atoms, and consequently improve the hardness and resistance to the external shear stress. Therefore, the interaction between the metal atoms is similar to that between atoms in pure metal crystals. The evaluated material would undergo permanent deformation because of the interactions between the metal atoms. The hardness of pure metals is often low at approximately 1–2 GPa because the lack of strong ionic or covalent bonds in a metal limits the slipping region of electrons, which also leads to limited hardness improvement resulting from metal bonds in metal crystals.

4. Conclusions

Mn_3N_2 gives us a perspective to understand the difference between the predictions by the hardness models and the tested results. Here, we synthesized high-quality, single-phase bulk Mn_3N_2 samples using HTHP synthesis, and the measured Vickers hardness was 9.9 GPa. By comparing the predicted value of hardness model with the experimental value, we found that the actual hardness of the sample was higher than the theoretical prediction. We investigated the electronic structures of Mn_3N_2 using first-principle simulations and found that the *d* orbital electrons in Mn–Mn form a path for the current and can effectively improve the hardness of this crystal. Therefore, the commonly observed electron slippage between TM–TM enhances the hardness of the crystals owing to its covalent bonding-like properties, on the premise that ionic bonds act as a “skeleton” in the crystals of TMLEs. The underestimated impact of the TM–TM bonds on the hardness and methods for optimizing these bonds by introducing LE atoms may assist in the design of modern alloy materials with enhanced hardness values.

Author Contributions: Data curation, S.Z., G.S. and Z.W.; Formal analysis, X.W., K.B., P.Z., X.Z., Q.T., Y.G. and T.C.; Funding acquisition, T.C.; Resources, P.Z.; Software, C.Z. and J.Z.; Writing—original draft, S.Z.; Writing—review and editing, S.Z. All authors have read and agreed to the published version of the manuscript.

Funding: This research was funded by the National Key R&D Program of China (2018YFA0703404 and 2017YFA0403704), the National Natural Science Foundation of China (11774121 and 91745203), the National Key Research and Development Program of China (2016YFB0201204), and the Program for Changjiang Scholars and Innovative Research Team in University (IRT_15R23).

Data Availability Statement: The data that support the findings of this study are available from the corresponding author upon reasonable request.

Acknowledgments: Parts of calculations were performed in the High Performance Computing Center (HPCC) of Jilin University.

Conflicts of Interest: The authors declare no conflict of interest.

References

1. Chen, X.Q.; Niu, H.; Li, D.; Li, Y. Modeling hardness of polycrystalline materials and bulk metallic glasses. *Intermetallics* **2011**, *19*, 1275–1281. [[CrossRef](#)]
2. Gao, F.M.; He, J.; Wu, E.; Liu, S.; Yu, D.; Li, D.; Zhang, S.; Tian, Y. Hardness of covalent crystals. *Phys. Rev. Lett.* **2003**, *91*, 015502. [[CrossRef](#)] [[PubMed](#)]
3. Guo, X.J.; Li, L.; Liu, Z.; Yu, D.; He, J.; Liu, R.; Xu, B.; Tian, Y.; Wang, H.-T. Hardness of covalent compounds: Roles of metallic component and *d* valence electrons. *J. Appl. Phys.* **2008**, *104*, 023503. [[CrossRef](#)]
4. Li, Q.; Zhou, D.; Zheng, W.; Ma, Y.; Chen, C. Anomalous Stress Response of Ultrahard WBn Compounds. *Phys. Rev. Lett.* **2015**, *115*, 185502. [[CrossRef](#)]
5. Chung, H.Y.; Weinberger, M.B.; Yang, J.M.; Tolbert, S.H.; Kaner, R.B. Correlation between hardness and elastic moduli of the ultraincompressible transition metal diborides RuB_2 , OsB_2 , and ReB_2 . *Appl. Phys. Lett.* **2008**, *92*, 261904. [[CrossRef](#)]
6. Weinberger, M.B.; Levine, J.B.; Chung, H.; Cumberland, R.W.; Rasool, H.I.; Yang, J.-M.; Kaner, R.B.; Tolbert, S.H. Incompressibility and Hardness of Solid Solution Transition Metal Diborides: $Os_{1-x}Ru_xB_2$. *Chem. Mater.* **2009**, *21*, 1915–1921. [[CrossRef](#)]

7. Liang, Y.; Zhang, B. Mechanical and electronic properties of superhard ReB₂. *Phys. Rev. B* **2007**, *76*, 132101. [[CrossRef](#)]
8. Zhang, Y.; Zhao, D.Q.; Pan, M.X.; Wang, W.H. Glass forming properties of Zr-based bulk metallic alloys. *J. Non-Cryst. Solids* **2003**, *315*, 206–210. [[CrossRef](#)]
9. Gou, H.Y.; Hou, L.; Zhang, J.; Gao, F. Pressure-induced incompressibility of ReC and effect of metallic bonding on its hardness. *Appl. Phys. Lett.* **2008**, *92*, 241901. [[CrossRef](#)]
10. Fu, H.Z.; Peng, W.M.; Gao, T. Structural and elastic properties of ZrC under high pressure. *Mater. Chem. Phys.* **2009**, *115*, 789–794. [[CrossRef](#)]
11. Simunek, A. Vickers hardness of Ru-, Ta-, W-, Re-, Os-, and Ir carbides and nitrides calculated by the bond strength method. *MRS Commun.* **2022**, *12*, 759–761. [[CrossRef](#)]
12. Zhang, R.F.; Legut, D.; Niewa, R.; Argon, A.S.; Veprek, S. Shear-induced structural transformation and plasticity in ultraincompressible ReB₂ limit its hardness. *Phys. Rev. B* **2010**, *82*, 104104. [[CrossRef](#)]
13. Chen, X.Q.; Fu, C.L.; Krčmar, M.; Painter, G.S. Electronic and structural origin of ultraincompressibility of 5d transition-metal diborides MB₂ (M = W, re, os). *Phys. Rev. Lett.* **2008**, *100*, 196403. [[CrossRef](#)] [[PubMed](#)]
14. Chung, H.Y.; Weinberger, M.B.; Levine, J.B.; Kavner, A.; Yang, J.M.; Tolbert, S.H.; Kaner, R.B. Synthesis of ultra-incompressible superhard rhenium diboride at ambient pressure. *Science* **2007**, *316*, 436–439. [[CrossRef](#)] [[PubMed](#)]
15. Haines, J.; Leger, J.M.; Bocquillon, G. Synthesis and design of superhard materials. *Annu. Rev. Mater. Res.* **2001**, *31*, 1–23. [[CrossRef](#)]
16. Yao, H.Z.; Ouyang, L.Z.; Ching, W.Y. Ab initio calculation of elastic constants of ceramic crystals. *J. Am. Ceram. Soc.* **2007**, *90*, 3194–3204. [[CrossRef](#)]
17. Akrami, S.; Edalati, P.; Fuji, M.; Edalati, K. High-entropy ceramics: Review of principles, production and applications. *Mater. Sci. Eng. R-Rep.* **2021**, *146*, 100644. [[CrossRef](#)]
18. Miracle, D.B.; Senkov, O.N. A critical review of high entropy alloys and related concepts. *Acta Mater.* **2017**, *122*, 448–511. [[CrossRef](#)]
19. Ningthoujam, R.S.; Gajbhiye, N.S. Synthesis, electron transport properties of transition metal nitrides and applications. *Prog. Mater. Sci.* **2015**, *70*, 50–154. [[CrossRef](#)]
20. Feng, X.; Bao, K.; Tao, Q.; Li, L.; Shao, Z.; Yu, H.; Xu, C.; Ma, S.; Lian, M.; Zhao, X.; et al. Role of TM-TM Connection Induced by Opposite d-Electron States on the Hardness of Transition-Metal (TM = Cr, W) Mononitrides. *Inorg. Chem.* **2019**, *58*, 15573–15579. [[CrossRef](#)]
21. Yu, R.; Chong, X.; Jiang, Y.; Zhou, R.; Yuan, W.; Feng, J. The stability, electronic structure, elastic and metallic properties of manganese nitrides. *RSC Adv.* **2015**, *5*, 1620–1627. [[CrossRef](#)]
22. Zhang, Z.; Mi, W. Progress in ferrimagnetic Mn₄N films and its heterostructures for spintronics applications. *J. Phys. D Appl. Phys.* **2021**, *55*, 013001. [[CrossRef](#)]
23. Lei, L.; Hong, X.; Fangfang, L.; Yongqiang, Z.; Bin, B.; Kezhao, L. Preparation and Characteristics of Uranium Nitride Thin Films. *Rare Met. Mater. Eng.* **2015**, *44*, 1975–1978.
24. Rognerud, E.G.; Rom, C.L.; Todd, P.K.; Singstock, N.R.; Bartel, C.J.; Holder, A.M.; Neilson, J.R. Kinetically Controlled Low-Temperature Solid-State Metathesis of Manganese Nitride Mn₃N₂. *Chem. Mater.* **2019**, *31*, 7248–7254. [[CrossRef](#)]
25. Yin, W.W.; Lei, L.; Jiang, X.; Liu, P.; Liu, F.; Li, Y.; Peng, F.; He, D. High pressure synthesis and properties studies on spherical bulk epsilon-Fe₃N. *High Press. Res.* **2014**, *34*, 317–326. [[CrossRef](#)]
26. Lei, L.; Zhang, L.; Gao, S.; Hu, Q.; Fang, L.; Chen, X.; Xia, Y.; Wang, X.; Ohfuji, H.; Kojima, Y.; et al. Neutron diffraction study of the structural and magnetic properties of epsilon-Fe₃N_{1.098} and epsilon-Fe_{2.322}CO_{0.678}N_{0.888}. *J. Alloy. Compd.* **2018**, *752*, 99–105. [[CrossRef](#)]
27. Wang, S.M.; Yu, X.; Zhang, J.; Wang, L.; Leinenweber, K.; He, D.; Zhao, Y. Synthesis, Hardness, and Electronic Properties of Stoichiometric VN and CrN. *Cryst. Growth Des.* **2016**, *16*, 351–358. [[CrossRef](#)]
28. Chen, M.; Wang, S.; Zhang, J.; He, D.; Zhao, Y. Synthesis of Stoichiometric and Bulk CrN through a Solid-State Ion-Exchange Reaction. *Chem. A Eur. J.* **2012**, *18*, 15459–15463. [[CrossRef](#)]
29. Blochl, P.E. Projector augmented-wave method. *Phys. Rev. B Condens. Matter* **1994**, *50*, 17953–17979. [[CrossRef](#)]
30. Kresse, G.; Furthmüller, J. Efficient iterative schemes for ab initio total-energy calculations using a plane-wave basis set. *Phys. Rev. B Condens. Matter* **1996**, *54*, 11169–11186. [[CrossRef](#)]
31. Perdew, J.P.; Burke, K.; Ernzerhof, M. Generalized gradient approximation made simple. *Phys. Rev. Lett.* **1996**, *77*, 3865–3868. [[CrossRef](#)] [[PubMed](#)]
32. Steinberg, S.; Dronskowski, R. The Crystal Orbital Hamilton Population (COHP) Method as a Tool to Visualize and Analyze Chemical Bonding in Intermetallic Compounds. *Crystals* **2018**, *8*, 225. [[CrossRef](#)]
33. Mueller, P.C.; Ertural, C.; Hempelmann, J.; Dronskowski, R. Crystal Orbital Bond Index: Covalent Bond Orders in Solids. *J. Phys. Chem. C* **2021**, *125*, 7959–7970. [[CrossRef](#)]
34. Toby, B.H. EXPGUI, a graphical user interface for GSAS. *J. Appl. Crystallogr.* **2001**, *34*, 210–213. [[CrossRef](#)]
35. Zhang, L.J.; Wang, Y.; Lv, J.; Ma, Y. Materials discovery at high pressures. *Nat. Rev. Mater.* **2017**, *2*, 17005. [[CrossRef](#)]